

# Neural networks and separation of background and foregrounds in astrophysical sky maps

C. Baccigalupi<sup>1</sup>, L. Bedini<sup>2</sup>, C. Burigana<sup>3</sup>, G. De Zotti<sup>4</sup>, A. Farusi<sup>2</sup>, D. Maino<sup>5</sup>, M. Maris<sup>5</sup>, F. Perrotta<sup>1</sup>, E. Salerno<sup>2</sup>, L. Toffolatti<sup>6</sup>, A. Tonazzini<sup>2</sup>

<sup>1</sup>SISSA/ISAS, Astrophysics Sector, Via Beirut, 4, I-34014 Trieste, Italy. Email bacci@sissa.it, perrotta@sissa.it

<sup>2</sup>IEI-CNR, Via Alfieri, 1, I-56010 Ghezzano, Pisa, Italy. Email <name>@iei.pi.cnr.it

<sup>3</sup>TeSRE-CNR, Via Gobetti, 101, I-40129 Bologna, Italy. Email burigana@tesre.bo.cnr.it

<sup>4</sup>Oss. Astr. Padova, Vicolo dell’Osservatorio 5, 35122 Padova, Italy. Email dezotti@pd.astro.it

<sup>5</sup>Oss. Astr. Trieste, Via G.B. Tiepolo, 11, I-34131 Trieste, Italy. Email maino@ts.astro.it, maris@ts.astro.it

<sup>6</sup>Dpto. de Física, c. Calvo Sotelo s/n, 33007 Oviedo, Spain Email toffol@pinon.ccu.uniovi.es

2 December 2024

## ABSTRACT

The Independent Component Analysis (ICA) algorithm is implemented as a neural network for separating signals of different origin in astrophysical sky maps. Due to its self-organizing capability, it works without prior assumptions on the signals, neither on their frequency scaling, nor on the signal maps themselves; instead, it learns directly from the input data how to separate the physical components, making use of their statistical independence.

To have a first insight into the capabilities of this approach, we apply the ICA algorithm on sky patches, taken from simulations and observations, at the microwave frequencies, that are going to be deeply explored in a few years on the whole sky, by the Microwave Anisotropy Probe (MAP) and by the PLANCK Surveyor Satellite. The maps are at the frequencies of the Low Frequency Instrument (LFI) aboard the PLANCK satellite (30, 44, 70 and 100 GHz), and contain simulated astrophysical radio sources, Cosmic Microwave Background (CMB) radiation, and Galactic diffuse emissions from thermal dust and synchrotron. We show that the ICA algorithm is able to recover each signal, with precision going from 10% for the Galactic components to percent for CMB; radio sources are almost completely recovered down to a flux limit corresponding to  $0.7\sigma_{CMB}$ , where  $\sigma_{CMB}$  is the rms level of CMB fluctuations. The signal recovering possesses equal quality on all the scales larger than the pixel size. In addition, we show that the frequency scalings of the input signals can be partially inferred from the ICA outputs, at the percent precision for the dominant components, radio sources and CMB.

Standing on these encouraging results, we believe that algorithms as the one presented here should be considered in the near future as a viable tool into the science of components separation in astrophysical observations.

## 1 INTRODUCTION

Observing the sky in any frequency band implies to observe the superposition of several signals, coming from different processes emitting radiation along the line of sight.

A good example of this situation is what we see in the microwave range. Going from nearby to far emitted radiation, in our observations we find first the Galactic contribution from about 20 Kelvin thermal dust and electromagnetic scattering between charged particles, second the signals from other galaxies, third cosmological signals provided by the Cosmic Microwave Background (CMB) radiation and its interaction with galaxy clusters before reaching us.

Of course we want to study these signals singularly since they cover wide interesting scientific aspects in astrophysics.

The basis for this should be to apply to the observed sky maps some algorithm able to separate the different components. This is made possible only by having a number of different sky maps at different frequencies; in these conditions, one could hope to employ some appropriate image analysis tool from computer science in astrophysics, recovering with the best possible accuracy the different signals composing the images performed on all the observation frequencies.

Again, the microwave electromagnetic band represents an interesting example of these issues. As we already mentioned, one of the most important astrophysical targets in the next decade will be the exploration of the electromagnetic spectrum in the microwave range, because in this spectral region the CMB is the dominant component. The study of the relic radiation from the Big Bang is a central topic in

the present physical research, since it carries detailed information regarding almost all the open problems in cosmology. This information is encoded into the CMB anisotropies perturbing the whole sky temperature  $T \simeq 3K$ ; they were first discovered in 1992 at the level  $\delta T/T \simeq 10^{-5}$  aboard the COBE satellite (Smoot et al. 1992) on angular scales larger than about  $10^\circ$ . Soon after this discovery, it was realized that a substantial amount of the CMB physical information had to be obtained by analyzing the anisotropies on degree and sub-degree angular scales. The reason is that the photon-baryon fluid sound horizon, at the time at which CMB radiation originated, subtended roughly one degree in the sky; the sub-horizon acoustic oscillations in the cosmic fluid are strictly dependent on the main cosmological parameters, as well as on the nature and statistics of this early stage of cosmological perturbations (see Turner & Tyson 1999 for reviews). For these reasons, in a few years the Microwave Anisotropy Probe (MAP) (Bennet et al. 1996) and the PLANCK Surveyor satellite (Mandolesi et al. 1998; Puget et al. 1998) experiments will explore the CMB anisotropies on the whole sky at the level  $\delta T/T \simeq 10^{-6}$  and on scales of about 10 arcminutes. Together with CMB science, another challenge for these missions is to perform the most accurate full sky surveys of the Galactic and extra Galactic foregrounds at microwave frequencies, since the satellites will operate at several frequency channels. In particular, PLANCK will observe the sky on 9 frequency channels from 30 to 900 GHz (Mandolesi et al. 1998; Puget et al. 1998). There is presently a great deal of work to study the existing database on the foregrounds of various nature, as well as developing data analysis tools (see e.g. Tegmark 1999 and references therein). The problem of maps denoising has been faced with the wavelets analysis on the whole sphere (Tenorio et al. 1999) and on sky patches (Sanz et al. 1999b). Moreover, algorithms to separate background and foregrounds once knowing their sum in the different frequency channels have been developed (Bouchet et al. 1998; Hobson et al. 1998). In these works, component separation techniques like Wiener filtering (WF) and maximum entropy method (MEM) are applied to simulated data from the PLANCK satellite, taking into account the expected instrumental features. Assuming perfect knowledge of the frequency scaling laws of all the components, as well as priors on the statistical properties of the signals spatial pattern, these algorithms are able to recover the signals from the strongest components, at the best PLANCK resolution of about 10 arcminutes.

We follow here a rather different strategy by studying a tool completely dedicated to the separation of the components. We consider signal denoising and component separation as separated steps into the data analysis phase; this relaxes the request to make the two aspects with one algorithm only, and allows for the scientific study and specialization of each aspect separately.

The algorithm we first analyze here is the Independent Component Analysis (ICA), that we implement as a neural network; it works in a markedly different way with respect to the WF and MEM approaches. We anticipate here the basic concepts. In WF and MEM the inversion problem to obtain the components from the data can be written and solved by using the prior knowledge assumed for frequency scalings and signals spatial patterns. On the contrary, a neural network algorithm possesses a self-organizing structure,

and is able to approach the final result even if the priors are absent; despite of this apparent lack of information, the ICA method exploits the independence of the signals composing the observed maps and is able to recover, up to a certain accuracy, each signal component multiplied by an overall constant.

We adopt in this first paper a “blind” strategy, in other words we do not help the ICA algorithm to make its job in any way, obtaining even in these extreme conditions very encouraging results. Of course this will be not the case of a real experiment, since one has some knowledge of what he’s going to observe; for example, in the case of the CMB experiments we should possess at least an approximation of the frequency scaling of the foregrounds – rather well known for the CMB itself (Fixsen et al. 1996; Mather et al. 1999) –, as well as maps of several observed regions at frequencies near to the PLANCK satellite operations.

The substantial part of this paper is dedicated to formalize our problem and to introduce the ICA algorithm in an astrophysical context, remaining as general as possible, and not referring to any experiment in particular; indeed, as we mentioned in the beginning of this Introduction, in most cases an astrophysical observation produces a map with several components added, whose properties both for frequency scalings and spatial pattern are only approximately known or totally unknown. We believe that an algorithm able to learn by itself the independent components present in the observed maps like the ICA method could be useful in many of these problems.

The paper is organized as follows. In Section II we define our problem in a formal way and we briefly recall the approaches adopted in previous works; In Section III we describe the ICA algorithm; in Section IV we describe our database and in Section V we present our analysis technique and results; in Section VI we draw the concluding remarks and list some future developments.

## 2 FORMALISM AND PREVIOUS APPROACHES

We will give here the basic definitions for the quantities we will use throughout the paper, together with a brief description of the previously proposed methods for the present problem.

Let us first formalize our separation problem by assuming that each radiation source, generally a function of both the position in the sky,  $(\xi, \eta)$ , and of frequency,  $\nu$ , can be separated into the product of a function of the position and a function of the frequency. Let us also assume that we have  $N$  source functions, and that the angular coordinates  $\xi$  and  $\eta$  can be treated as Cartesian coordinates. This is not a limiting assumption, and is justified if we only consider small patches of the sky. The generic source function will thus be

$$\tilde{s}_i(\xi, \eta, \nu) = s_i(\xi, \eta) \cdot \mathcal{F}_i(\nu) \quad i = 1, \dots, N \quad (1)$$

The total radiation received in the point  $(\xi, \eta)$  in the sky will be

$$\tilde{x}(\xi, \eta, \nu) = \sum_{i=1}^N s_i(\xi, \eta) \cdot \mathcal{F}_i(\nu) \quad (2)$$

Let us suppose that the measuring instrument has  $M$  channels, with frequency responses  $t_j(\nu)$ ,  $j = 1, \dots, M$  centered on different frequency values, and that the beam patterns are independent of frequency within each channel passband. Let us denote these beam patterns by means of the space-invariant PSF's  $h_j(\xi, \eta)$ , thus assuming measured maps produced by a linear convolutional mechanism. This does not correspond to the real situation, where elliptical beam patterns are expected, and, due to the particular scan strategy of the experiment, a space-variant defocusing will be obtained. From the above assumptions and from equation (2), it is easy to see that the map produced at the  $j$ -th channel will be:

$$x_j(\xi, \eta) = \int h_j(\xi - x, \eta - y) t_j(\nu) \cdot \sum_{i=1}^N s_i(x, y) \mathcal{F}_i(\nu) dx dy d\nu + \epsilon_j(\xi, \eta) = \tilde{x}_j(\xi, \eta) * h_j(\xi, \eta) + \epsilon_j(\xi, \eta), \quad j = 1, \dots, M, \quad (3)$$

where:

$$\tilde{x}_j(\xi, \eta) = \sum_{i=1}^N a_{ji} \cdot s_i(x, y), \quad j = 1, \dots, M, \quad (4)$$

$$a_{ji} = \int \mathcal{F}_i(\nu) t_j(\nu) d\nu, \quad j = 1, \dots, M; i = 1, \dots, N, \quad (5)$$

\* denotes linear convolution and  $\epsilon_j(\xi, \eta)$  represents the instrumental noise. Equation (4) can also be written in matrix form:

$$\tilde{\mathbf{x}}(\xi, \eta) = A \mathbf{s}(\xi, \eta) \quad (6)$$

where the entries of the  $M \times N$  matrix  $A$  are given by Equation 5.

The unknowns of our problem are the  $N$  functions  $s_i(\xi, \eta)$ , and the data set is made of the  $M$  maps  $x_j(\xi, \eta)$  in equation (3). Besides the measured data, we also know exactly the instrument beam-patterns  $h_j(\xi, \eta)$ , and, more or less approximately (depending on the specific source), the coefficients  $a_{ji}$  in system (4).

Equation (3) can be easily rewritten in the Fourier space:

$$X_j(\omega_\xi, \omega_\eta) = \sum_{i=1}^N R_{ji}(\omega_\xi, \omega_\eta) S_i(\omega_\xi, \omega_\eta) + \mathcal{E}_j(\omega_\xi, \omega_\eta), \quad (7)$$

where the capital letters denote the Fourier transforms of the corresponding lowercase functions, and

$$R_{ji}(\omega_\xi, \omega_\eta) = \mathcal{H}_j(\omega_\xi, \omega_\eta) a_{ji}, \quad (8)$$

being  $\mathcal{H}_j$  the Fourier transform of the beam profile  $h_j$ .

Equation (7) can thus be rewritten in matrix form:

$$\mathbf{X} = R \mathbf{S} + \mathcal{E}. \quad (9)$$

The above equation must be satisfied at each Fourier mode  $(\omega_\xi, \omega_\eta)$ , independently. The aim is to recover the true signals  $S_i(\omega_\xi, \omega_\eta)$  constituting the column vector  $\mathbf{S}$ . If the matrix  $A$  in (6) is exactly known, then in absence of the noise,

the problem would then be reduced to that of a linear inversion of eq.(9) at each Fourier mode; in the realistic case, however, such inversion would carry a wrong result of course, and one should perform an approximate inversion based on statistical approaches built on *a priori* knowledge on the signals to recover. In the following two subsections we briefly describe such approaches, and in the last one we briefly recall a tool so far dedicated mostly to the denoising problem. In the next Section we introduce our algorithm, that works on real space instead of the Fourier one.

## 2.1 The maximum entropy approach

The Maximum Entropy Method (MEM) for the reconstruction of images is based on a Bayesian approach to the problem; the theoretical foundations of this method are discussed in detail elsewhere (see Skilling et al. 1989).

Suppose that  $\mathbf{X}$  is a vector of  $M$  observations whose probability distribution  $P(\mathbf{X}|\mathbf{S})$  depends on the values of  $N$  quantities  $\mathbf{S} = S_1, \dots, S_N$ . Let us indicate with  $P(\mathbf{S})$  the *prior* probability distribution of  $\mathbf{S}$ : it tells us what is known about  $\mathbf{S}$  without knowledge of the data. Given the observed data  $\mathbf{X}$ , the Bayes' theorem states that the conditional distribution of  $\mathbf{S}$  (the *posterior* distribution of  $\mathbf{S}$ ) is given by the product between the likelihood of the data,  $P(\mathbf{X}|\mathbf{S})$ , and the prior:

$$P(\mathbf{S}|\mathbf{X}) = z \cdot P(\mathbf{X}|\mathbf{S})P(\mathbf{S}), \quad (10)$$

where  $z$  is a normalization constant.

One is therefore induced to construct an estimator  $\hat{\mathbf{S}}$  of the true signal vector by maximizing the posterior probability  $P(\mathbf{S}|\mathbf{X}) \propto P(\mathbf{X}|\mathbf{S})P(\mathbf{S})$ . However, while the likelihood in (10) is quite simple to determine once the noise and signals covariance matrix are known, a major problem in the Bayesian approach consists in the appropriate choice of the prior distribution for the model considered: because Bayes' theorem is simply a rule for manipulating probabilities, it cannot by itself help us to assign them in the first place, so one has to look elsewhere. The Maximum Entropy principle is a consistent variational method for the assignment of probabilities under certain types of constraints that must refer to the probability distribution directly.

The principle of Maximum Entropy states that if one has some information  $I$  on which the probability distribution is based, one can assign a probability distribution to a proposition  $i$  such that  $P(i|I)$  contains only the information  $I$  that one actually possesses. This assignment is done by maximizing the Entropy

$$H \equiv - \sum_{i=1}^N P(i|I) \log P(i|I) \quad (11)$$

It can be seen that when nothing is known except that the probability distribution should be normalized, the Maximum Entropy principle reduces to the uniform prior. In our case the proposition  $i$  represents  $\mathbf{S}$ , and the information  $I$  is the assumption of signal statistical independence. In this way we can assign the prior probability to the image vector  $\mathbf{S}$ ; this was done in the case in which it is strictly positive (see Skilling et al. 1989); however, temperature fluctuations in the cosmic microwave background can assume both positive and negative values; a generalization of this prior to

non-positive definite images has been performed in a recent work (Hobson et al. 1998), where the starting idea was to express the signal as the difference between two strictly positive distributions. This extension allowed the MEM to be applied to a wide range of astronomical image reconstruction problems, in particular the separation of components in images simulating the ones that will be produced by the forthcoming MAP and PLANCK experiments (Hobson et al. 1998). The construction of the entropic prior requires, in general, the perfect knowledge of the frequency scaling behavior of the components to be reconstructed, and in addition the signals covariance matrix  $\mathbf{C}(\mathbf{k}) = \langle \mathbf{S}(\mathbf{k})\mathbf{S}^\dagger(\mathbf{k}) \rangle$ .

## 2.2 The multifrequency Wiener filtering

If one assumes that the emission associated to each physical component is well described by a Gaussian random field, thus adopting a Gaussian prior rather than an entropic prior, the Bayesian approach gives rise to a straightforward derivation of the multifrequency Wiener filtering method (Bouchet et al. 1998); also in this case, an estimator of the signal vector is obtained by maximizing the posterior probability in (10), in terms of the signals covariance matrix  $\mathbf{C}(\mathbf{k})$ .

The Gaussian prior probability distribution for the signal has the form

$$P(\mathbf{s}) \propto \exp(-\mathbf{S}^\dagger \mathbf{C}^{-1} \mathbf{S}) . \quad (12)$$

The obtained signal estimator can be expressed in terms of the Wiener matrix  $\mathbf{W} \equiv (\mathbf{C}^{-1} + \mathbf{R}^\dagger \mathbf{N}^{-1} \mathbf{R})^{-1}$ , where  $\mathbf{R}$  corresponds to the matrix in (9) and  $\mathbf{N}(\mathbf{k}) = \langle \boldsymbol{\epsilon}(\mathbf{k})\boldsymbol{\epsilon}^\dagger(\mathbf{k}) \rangle$  is the noise covariance matrix, in a linear relation that contains the data vector,

$$\hat{\mathbf{S}} = \mathbf{W} \mathbf{X} . \quad (13)$$

The  $\mathbf{W}$  matrix has the role of a linear filter; again, its construction requires an *a priori* knowledge of the spectral behavior of the signals.

For purely Gaussian signals, the reconstructed estimators can thus be compared with the simulated ones (Bouchet et al. 1998). On the other hand, it is well known that the hypothesis of a Gaussian fluctuation field behavior is not reliable for most of the signal components (except for the pure CMB signal and the white noise); the choice of an entropic prior renounce to this simplified fluctuation model, and is able to reproduce the Wiener filtering results for a Gaussian prior (Hobson et al. 1998).

The results of applying the MEM and WF to the simulated PLANCK maps are shown in detail elsewhere (Bouchet et al. 1998; Hobson et al. 1998), and we just summarize them. Both WF and MEM make use of the exact knowledge of the frequency dependence of the components; as the assumptions about the spatial distribution are concerned, two different situations have been tested: in one case, the component separation was performed by making use of the supposedly known covariance matrix, and the algorithm recovered the simulated maps with good accuracy; in the other situation, the covariance matrix was assumed to describe flat spectra for all the components, knowing only their true normalization; the methods were applied iteratively by updating the covariance matrix at each step; in the last case the reconstruction was not much worse than in the first one. Independently of the prior information used, the CMB power

spectrum was in general reproduced more accurately than the foregrounds. In general the MEM reveals to work better than the linear Wiener filtering, particularly for highly non-Gaussian and weak signals.

## 2.3 The wavelet analysis

Development of wavelet techniques applied to signal processing has been very fast in the last ten years (see, e.g., Jawerth et al. 1994). The wavelet approach is conceptually very simple: whereas the Fourier transform is highly inefficient in dealing with the local behavior, the wavelet transform is able to introduce a good space-frequency localization, thus providing information on the contributions coming from different positions and scales.

In one dimension, we can define the *analyzing* wavelet as  $\Psi(x; R, b) \equiv R^{-1/2} \psi(\frac{x-b}{R})$ , dependent on two parameters, dilation ( $R$ ) and translation ( $b$ ), and  $\psi(x)$  is a one-dimensional function satisfying the following conditions: a)  $\int_{-\infty}^{\infty} dx \psi(x) = 0$ , b)  $\int_{-\infty}^{\infty} dx \psi^2(x) = 1$  and c)  $\int_{-\infty}^{\infty} dk |k|^{-1} \psi^2(k) < \infty$ , where  $\psi(k)$  is the Fourier transform of  $\psi(x)$ . The wavelet  $\Psi$  operates as a mathematical microscope of magnification  $R^{-1}$  at the space point  $b$ . The wavelet coefficients associated to a one-dimensional function  $f(x)$  are:

$$w(R, b) = \int dx f(x) \Psi(x; R, b) . \quad (14)$$

As regards 2-dimensional images, the wavelet analysis can be performed following different approaches. The two computationally faster algorithms are the ones based on Multiresolution analysis (Mallat 1989) and on 2D wavelet analysis (Lemarié & Meyer 1986), using tensor products of one dimensional wavelets. The discrete Multiresolution analysis entails the definition of a one-dimensional *scaling* function  $\phi$ , normalized as  $\int_{-\infty}^{\infty} dx \phi(x) = 1$  (Ogden et al. 1997). Scaling functions act as low-pass filters whereas wavelet functions single out one scale. The 2D wavelet method (Sanz et al. 1999b) is based on two scales, providing therefore more information on different resolutions (defined by the product of the two scales) than the Multiresolution one.

Recently, wavelet techniques have been introduced in the analysis of CMB data. Denoising of CMB maps has been performed on patches of the sky of  $12^\circ.8 \times 12^\circ.8$  using either multiresolution techniques (Sanz et al. 1999a) and 2D wavelets (Sanz et al. 1999b), as well as on the whole celestial sphere (Tenorio et al. 1999). As a first approach, maps with cosmological signal plus instrumental Gaussian noise have been considered. The separation of the different astrophysical components from the CMB signal being the goal of future applications.

Denoising of CMB maps has been carried out by using a signal-independent prescription, the SURE thresholding method (Donoho et al. 1995). The results are model independent and only a good knowledge of the noise affecting the observed CMB maps is required, whereas nothing has to be assumed on the nature of the underlying field(s). Moreover, wavelet techniques are highly suitable to localize noise variations and map features in presence of non-uniform noise.

The wavelet method is able to reconstruct CMB maps

with an error improvement factor between 3 and 5. For comparison, the  $C_\ell$ s of the denoised maps obtained applying Wiener filter have relative errors a factor of about 2 larger than the relative errors of the  $C_\ell$ s obtained from the wavelet reconstructed maps.

Wavelets have also been applied to the detection of point sources in CMB maps in presence of cosmological signal (Cayón et al. 2000), diffuse galactic foregrounds and instrumental noise (Tenorio et al. 1999). Provided that the beam pattern is known, the convolution of the CMB map with a wavelet of the same scale and similar shape will produce wavelet coefficients with maxima (amplification) at the position of point sources (location). This detection technique gives results comparable to the ones obtained by the filtering method presented previously (Tegmark & de Oliveira-Costa 1998). However, this latter method assumes that all the underlying fields are Gaussian.

Moreover, based on the analytical knowledge of the wavelet coefficients at the positions dominated by point sources, it is possible to recover the flux of the detected point sources with errors in the flux estimation below 25%.

### 3 THE ICA APPROACH

We introduce here a rather different approach, with capability to work “blindly” i.e. without knowledge of frequency and spatial properties of the signals to separate. Blind source separation is a very important aspect of many signal and image processing applications (Amari et al. 1998). The problem arises whenever a number of source signals are detected by multiple transducers, and the transmission channels for the sources are unknown, so that each transducer receives a mixture of the source signals with unknown scaling coefficients and channel distortion.

Several solutions have been proposed for this problem, each based on more or less sound principles, not all of which being typical of classical signal processing. Indeed, information theory, neural networks, statistics and probability have played an important part in the development of these techniques.

The treatment adopted here for this problem follows the one introduced in previous works (Amari et al. 1998; Bell et al. 1995), but limited to simple linear combinations of unconvolved source signals, that is the aspect we are interested in here.

The problem can be stated as follows: a set of  $N$  independent signals, functions of space, is input to an unknown frequency dependent multiple-input-multiple-output linear instantaneous system, whose  $M$  outputs are our observed signals. We use the term *instantaneous* to denote a system whose output at a given spatial point only depends on the input signals at the same point. Our objective is to find a stable *reconstruction system* to estimate the original input signals, in absence of any prior assumption neither on the signals distributions nor on their frequency scalings. The problem in its general form is normally unsolvable, and a “work hypothesis” must be made in order to proceed: the hypothesis we will make on our source signals is their mutual *statistical independence*, whatever their actual distributions. The necessary new concept with respect to previous approaches that we introduce here is the self-learning capa-

bility of the algorithm; indeed, in this blind approach it is necessary for the algorithm to learn directly from the data, by using the hypothesis of mutual independence of the signal components. A self-learning algorithm like this is commonly known as neural network and we will describe it below.

In the present work we do not consider specific instrumental features like beam convolution and noise contamination, leaving the specialization of the ICA method for specific experiments to future works; this allows us to highlight here the capabilities of this approach, able to work in conditions where other algorithms would be not viable. Therefore, we assume Equation (6) as our data model, just dropping the tilde accent on vector  $\mathbf{x}$ . Also, the presence of measurement noise appearing in Equation (7) will not be considered explicitly in this framework.

In order to recover the original source signals from the observed mixtures, we use a separating scheme in the form of a feed-forward neural network. The observed signals are input to an  $N \times M$  matrix  $W$ , referred to as the *the synaptic weight matrix*, whose adjustable entries,  $w_{ij}$ ,  $i = 1, \dots, N$ ,  $j = 1, \dots, M$ , are updated for every sample of the input vector  $\mathbf{x}(\xi, \eta)$  (at step  $\tau$ ) following a suitable *learning algorithm*. The output of matrix  $W$  at step  $\tau$  will be:

$$\mathbf{u}(\xi, \eta, \tau) = W(\tau)\mathbf{x}(\xi, \eta), \quad (15)$$

$W(\tau)$  is expected to converge to a true separating matrix, that is, a matrix whose output is a *copy* of the inputs, for every point  $(\xi, \eta)$ . Ideally, this final matrix  $W$  should be such that  $WA = I$ , where  $I$  is the  $N \times N$  identity. As an example, if  $M = N$ , it should be  $W = A^{-1}$ . There are, however, two basic indeterminacies in our problem: ordering and scaling. Even if we are able to extract  $N$  independent sources from  $M$  linear mixtures of them, we cannot know *a priori* the order in which they will be arranged, since this corresponds to unobservable permutations of the columns of matrix  $A$ . Moreover, the scales of the extracted signals are unknown, because when a signal is multiplied by some scalar constant, the effect is the same as of multiplying by the same constant the corresponding column of the mixing matrix. This means that  $W(\tau)$  will converge, at best, to a matrix  $W$  such that:

$$WA = PD, \quad (16)$$

where  $P$  is any  $N \times N$  permutation matrix, and  $D$  is a nonsingular diagonal scaling matrix. From Equations (6), (15) and (16) we thus have:

$$\mathbf{u} = W\mathbf{x} = WAs = PDs. \quad (17)$$

That is, as anticipated, each component of  $\mathbf{u}$  is a scaled version of a component of  $\mathbf{s}$ , not necessarily in the same order. We think this is not a serious inconvenience in our application, since we should be able to recover the proper scales for the separated sources from other informations, for example, matching with independent lower resolution observations as COBE for MAP and PLANCK. The performance of the separation algorithm is evaluated by means of matrix  $WA$ . If the separation is perfect, this matrix has only one nonzero element for each row and column. In any non-ideal situation each column of  $WA$  will be composed by non-zero numbers with a dominant one. We expect this to affect mostly the lower signals in our simulated maps, since their recovering is necessarily worse with respect to the dominant ones. This

has interesting consequences that we will describe in Section V.

In all the cases treated here, we will assume  $M \geq N$  but, in particular, we shall also consider the case where  $N$ , although smaller than  $M$ , is not known.

As already said, the basis we assumed for blind separation is the mutual statistical independence of the source signals. This can be expressed in terms of a separable joint probability density function  $q(\mathbf{s})$ :

$$q(\mathbf{s}) = \prod_{j=1}^N q_j(s_j) \quad (18)$$

where  $q_j(s_j)$  is the marginal probability density of the  $j^{\text{th}}$  source.

Various algorithms can be used to perform separation and to implement learning of matrix  $W$ . In general, a nonlinear transformation  $\mathbf{f}(\mathbf{u})$ , variously related to  $q(\mathbf{u})$ , is applied to the outputs of matrix  $W$ , and the result is used to optimize some suitably chosen function. This apparently innocent operation is indeed very powerful in manipulating the distribution of the outputs  $\mathbf{f}(\mathbf{u})$  and is a central point in the problems at hand here (Bell et al. 1995).

All these approaches can be derived from a unified principle based on the Kullback–Leibler (KL) divergence between the joint probability density of the output vector  $\mathbf{u}$ ,  $p_U(\mathbf{u})$ , and a function  $q(\mathbf{s})$ , which should be suitably chosen among the ones of the type (18). The KL divergence between the two functions mentioned above may be written as a function of matrix  $W$ , and can be considered as a cost function in the sense of Bayesian statistics:

$$R(W) = \int p_U(\mathbf{u}) \log \frac{p_U(\mathbf{u})}{q(\mathbf{u})} d\mathbf{u}. \quad (19)$$

It can be proved that  $R(W)$  has a global minimum, under mild conditions on  $q(\mathbf{u})$ , where  $W$  is such that  $WA = PD$ . The different possible choices for  $q(\mathbf{s})$  lead to the different particular learning strategies proposed in the literature (Amari et al. 1998; Yang et al. 1997).

The *uniform gradient* search method, which is a gradient-type algorithm, takes into account the non-Euclidean metric structure of our objective parameter space that is the set of all nonsingular matrices  $W$  (Amari et al. 1998). In a general  $M \geq N$  case, the following formula is derived:

$$W(\tau + 1) = W(\tau) - \alpha(\tau) [I - \mathbf{f}(\mathbf{u}(\tau))\mathbf{u}^T(\tau)] W(\tau), \quad (20)$$

being  $I$  the identity matrix. The convergence features of this iterative formula are shown to be independent of the particular matrix  $A$ , so that, even a strongly ill-conditioned system does not affect the convergence of the learning algorithm. In other words, even when contributions of some components are very small, there is no problem to recovering them. This desirable property is called the *equivariant property* since the asymptotic properties of the algorithms are independent of the mixing matrix and the scaling factors of the source signals. The  $\tau$ -dependent parameter  $\alpha$  is the so-called *learning rate*, and its value is normally decreased during the iterations, in other words each time that the algorithm reads all the map pixels. Regarding the choice of  $\alpha(\tau)$ , some criteria for learning this parameter and its annealing scheme are given elsewhere (Amari et al. 1998); we

have chosen  $\alpha(\tau)$  decreasing from  $10^{-3}$  to  $10^{-4}$  linearly with the number of iterations.

The final problem is how to choose the function  $\mathbf{f}(\mathbf{u})$ , or equivalently the marginal distributions  $q_j(u_j)$ . If we know the true source distributions, the best choice is to use them, since this gives the maximum likelihood estimator. However, the point is that when  $q_j(u_j)$  are specified incorrectly, the algorithm gives the correct answer under certain conditions. Suboptimal choices for the nonlinearities still allow the algorithm to perform separation: for sub-Gaussian source signals (negative kurtosis), we can select

$$f_i(u_i) = \beta u_i + u_i |u_i|^2, \quad (21)$$

and, for super-Gaussian source signals (positive kurtosis)

$$f_i(u_i) = \beta u_i + \tanh(\gamma u_i), \quad (22)$$

where  $\beta \geq 0$  and  $\gamma \geq 2$ . The situations where the observed signals contain mixtures of both sub-Gaussian and super-Gaussian sources are not considered here, although this will have to be done in the future.

A slightly different form of the learning algorithm in Equation (20) is shown to be able to separate an unknown number  $N$  of sources from  $M$  measurement channels (provided that  $M \geq N$ ) and indeed it is the one that we adopt (Amari et al. 1998):

$$W(\tau + 1) = W(\tau) + \alpha(\tau) \cdot [\Lambda - \mathbf{u}(\tau)\mathbf{u}^T(\tau) - \mathbf{f}(\mathbf{u}(\tau))\mathbf{u}^T(\tau)] W(\tau), \quad (23)$$

where  $\Lambda$  is a  $M \times M$  diagonal matrix:

$$\Lambda = \text{diag}[(u_1 + f_1(u_1))u_1] \dots [(u_M + f_M(u_M))u_M]. \quad (24)$$

We are almost ready to apply our algorithm, with the following operations. Pixel by pixel, the  $M \times M$  matrix  $W$  is multiplied by the  $M$ -vector  $\mathbf{x}$ , and gives vector  $\mathbf{u}$  as its output. This output is transformed through the nonlinear vector function  $\mathbf{f}(\mathbf{u})$ , and the result is combined with  $\mathbf{u}$  itself to build the update to matrix  $W$ , through Equation (23). After the maps have been read once, all the process has to be re-iterated to obtain the complete result.

We implemented our learning algorithm following equation (23), with the nonlinearities in (22), and  $\beta = 0$ ,  $\gamma = 2$ . As already stated, the mean of the input signal at each frequency is subtracted. In previous works (Yang et al. 1997) the initial matrix was chosen as  $W \propto I$ ; in that analysis, the image data consists in a set of components with nearly the same amplitude. The choice of the initial  $W$  influences of course the computation time, as well as the constants multiplying the reconstructed signals, and the order with which they are recovered; interestingly, we find useful to differentiate the diagonal elements in such a way that they roughly reflect the relative different weights of the various components in the resulting mixing, otherwise the algorithm takes more time to reach a good separation. For the problem at hand, the results shown in section 5 have been obtained starting from  $W = \text{diag}[1, 3, 30, 10]$ , for the case of a  $4 \times 4$   $W$ -matrix, and using only 20 learning steps: the time needed was about 1 minute on a UltraSparc machine, equipped with an 300 MHz UltraSparc processor, 256 MBytes RAM, running down SUN Solaris 7 Operating System, compiling the FORTRAN 90 code using SUN Fortran Workshop 5.0

In the next two Sections we give an application of the ICA method to partially simulated and observed data maps.

## 4 DATABASE

We describe here the components that sum up the sky signal, and that have to be separated by our algorithm.

The images are produced at four different observation frequencies, in correspondence to the four PLANCK LFI channels (Mandolesi et al. 1998), namely 30, 44, 70 and 100 GHz. The signals are shown in figure 1.

We made our map operations in the HEALPix sky pixelization scheme (see Górski et al. 1999). The sky patches we use have extension of about  $15^\circ \times 15^\circ$ , with pixel linear size  $3.5'$ ; the center position of the patches corresponds to medium galactic latitudes, namely  $l = 90^\circ$ ,  $b = 45^\circ$ .

Let us describe now the physical content in the patches. Our data are in antenna temperature (in  $\mu K$ ), which is the additive observable that we used in our maps.

The signal from the CMB has been derived by a flat Cold Dark Matter model (CDM,  $\Omega_{CDM} = .95$ ,  $\Omega_b = .05$ , three massless neutrinos species); the underlying fluctuations spectrum is Gaussian and scale invariant, with amplitude normalized to the COBE data (see Seljak & Zaldarriaga 1996). As it is well known, the CMB fluctuations exhibit a spectral law that can be conveniently described as follows:

$$s_{CMB}^{antenna}(\xi, \eta, \nu) = s_{CMB}^{thermod.}(\xi, \eta) \cdot \frac{\tilde{\nu}^2 e^{\tilde{\nu}}}{(e^{\tilde{\nu}} - 1)^2}, \quad (25)$$

where  $\tilde{\nu} = \frac{\nu}{56.8}$  and  $\nu$  is the frequency in GHz;  $s_{CMB}^{thermod.}(\xi, \eta)$  is essentially constant (Fixsen et al. 1996) with respect to the frequency while containing the whole coordinate dependence.

As Galactic foregrounds, we take synchrotron and thermal dust emissions. For the first one, we take the available observations at 408 MHz with about degree resolution (see Haslam et al. 1982), and assume that the temperature map depends on the frequency  $\nu$  as a simple power law:

$$\mathcal{F}_{syn} \propto \tilde{\nu}^{-n}, \quad (26)$$

where the spectral index is  $n = 2.9$ .

The angular distribution of the dust emission is taken from observational data IRAS+DIRBE at about 6 arcminutes resolution (see Schlegel et al. 1998). The frequency scaling is assumed to be described by the following spectral law:

$$\mathcal{F}_{dust} \propto \frac{\tilde{\nu}^{n+1}}{(e^{\tilde{\nu}} - 1)}, \quad (27)$$

with  $n = 2$ ; now  $\tilde{\nu}$  is  $h\nu/kT_{dust}$ :  $T_{dust}$  is the thermodynamical temperature of the dust, which depends on the position in the sky, so one would have to reconstruct the appropriate  $T_{dust}$  value pixel by pixel. The range of variation of  $T_{dust}$  in the sky is  $14 \div 25$  K; in the regions we consider,  $T_{dust}$  is approximately constant, oscillating at the percent level around  $18K$  that we assume to be valid on all our patch.

By limiting ourselves to the four LFI channels, we do not treat here the other Galactic foregrounds arising from electromagnetic interaction between charged free particles, the *free-free* emission, although it is a relevant component of the Galactic signal, and a possible source of contamination for the next CMB experiments (Mandolesi et al. 1998; Puget et al. 1998).

As extragalactic foreground, we use simulated maps of radio point sources obtained by a Poisson distribution according to the predicted number counts (Toffolatti et al.

1998). This contribution can be seen as an additional noise with an angular power spectrum essentially flat and variance decreasing with the frequency with a constant spectral index similar to the one of the dominant sources in that spectral region, that in terms of antenna temperature should be in the range (-2.3, -1.4). We simulate the radio source map at 100 GHz, and then we scale in frequency this signal with spectral index -1.9.

The input signal frequency scalings, normalized to 100 GHz, have been summarized in table (1).

## 5 BLIND ANALYSIS AND RESULTS

As is well known, the strongest signals at the PLANCK LFI frequency channels come from CMB and radio sources (although the latter are essentially a few high peaks), whereas synchrotron emission and thermal dust are roughly 1 or 2 orders of magnitude lower, depending on frequency. Nevertheless, such situation is good in this test phase of the ICA algorithm, either because the four signals exhibit very different spatial patterns and frequency scalings, and because it is interesting to check how the separation works with signals with markedly different amplitudes.

The simulated signals at the four frequencies are added to produce the physical maps to be treated by the ICA algorithm; also, the mean is set to zero in each channel. Our strategy is blind in this paper: no *a priori*, neither on the spatial statistics of the signals, nor on their frequency scalings, has been used in the separation process.

Let us now show the results. In figure 2 the final four maps have been shown. Several interesting features should be noted. The order of the plotted maps is permuted with respect to the input maps in figure 1, reflecting the order of the ICA outputs: the first output is synchrotron, the second represents radio sources, the third is CMB and the fourth is dust. All the maps appear very similar to the true ones, even synchrotron lower resolution pixels have been reproduced. In figures 3,5,4 and 6 we test the goodness of the separation by comparing power spectra and building scatter plots between the inputs and the outputs.

### 5.1 Signal recovery

For each map, we compute the angular power spectrum, defined by the expansion coefficients  $C_\ell$  of the two point correlation function in Legendre polynomials. As is well known, it can conveniently be expressed in terms of the coefficients of the expansion of the signal  $S$  into spherical harmonics,  $S(\theta, \phi) = \sum_{\ell m} a_{\ell m} Y_{\ell m}(\theta, \phi)$ :

$$C_\ell = \frac{1}{2\ell + 1} \sum_m |a_{\ell m}|^2. \quad (28)$$

Such coefficients are useful because from elementary properties of the Legendre polynomials it can be seen that the coefficient  $C_\ell$  quantifies the amount of perturbation on the angular scale  $\theta$  given by

$$\theta \simeq \frac{180}{\ell} \text{ degrees}. \quad (29)$$

Top left and right panels in figures 3,4, 5,6 show the power spectrum of the input and output signals respectively.

**Table 1.** Input signals frequency scalings.

frequency channel (GHz)	Radio sources	CMB	synchrotron	dust
100	1.00	1.00	1.00	1.00
70	1.97	1.14	2.81	.680
44	4.76	1.22	10.8	.351
30	9.86	1.26	32.8	.187

CMB exhibits the characteristic peaks on sub-degree angular scales resulting from the acoustic oscillations of the photon-baryon fluid at decoupling; the dashed line represents the theoretical model from which the map was generated, while the solid line is the power spectrum of our simulated patch: the difference between the two curves is due to the sample variance of the CMB Gaussian statistics. Radio sources are completely different, having all the power on small scales, reflecting the typical shot noise spatial pattern; dust and synchrotron emissions have power decreasing at small scales roughly as a power law, as expected (Mandolesi et al. 1998; Puget et al. 1998). Bottom left panels show the quality factor, defined as the ratio between true and reconstructed power spectrum coefficients, for each multipole  $\ell$ . The spectral region shown covers the power on all the scales below roughly 2 degrees. Bottom right panels are scatter plots of the ICA results: for each pixel of the maps, we plotted the value of the reconstructed image vs. the corresponding input value of the signal in that pixel.

These plots have been arranged to make clear the final products of the ICA algorithm. Reconstructed signals have zero mean and are in unit of  $d$ , that is the constant multiplying each output map, produced during the separation phase, as we mentioned in Section III. As we have shown, the scale of each signal is unreplicable for a blind separation algorithm like ICA. Nevertheless, a lot of information is encoded into the spatial pattern of each signals, and ultimately its overall normalization could be recovered by matching results from different experiments. Therefore, the relation between each true signal and its reconstruction will be

$$s_i^{in} = d \cdot s_i^{out} + b, \quad i = 1, \dots, N_{pixels}, \quad (30)$$

$b$  represents merely the mean of the input signal, that is zero for CMB and positive for the foregrounds. For clearness, we recover both  $d$  and  $b$  by performing a linear fit between the input and output maps  $s^{in}, s^{out}$  for each signal:

$$d = \frac{\sum_i s_i^{in} s_i^{out} - \bar{s}^{in} \cdot \sum_i s_i^{out}}{\sum_i (s_i^{out})^2 - \bar{s}^{out} \cdot \sum_i s_i^{out}}, \quad b = \bar{s}^{in} - d \cdot \bar{s}^{out}, \quad (31)$$

where the sums run over all the pixels, and the bar indicates the average value on the patch; the values of  $d$  and  $b$ , as well as the linear fits (dashed lines), are indicated for all the signals in the scatter plot panels. Also, in the same panels we show the standard deviation of the fit, that is

$$\sigma = \left[ \frac{1}{N_{pixels}} \sum_i (s_i^{in} - d \cdot s_i^{out} - b)^2 \right]^{1/2}. \quad (32)$$

A comparison of such quantity with respect to the input signals on the  $x$ -axis of the bottom right panels gives an estimation of the goodness of the reconstruction. From these graphs it is clear how the separation is more accurate for the strongest signals, independently of their spatial statistics.

CMB and radio sources are recovered with percent and 0.1% precision, respectively, while the level drops roughly to 10% for synchrotron and dust. In fact, the Galactic components appear to be slightly mixed; this may be adduced mainly to two causes: one is that these signals are subdominant at the LFI channels, so that the ICA algorithm does not reach the precision for CMB and radio sources (synchrotron receives contamination also from the radio sources, as it is evident in the scatter plot panel); the other is that a slight correlation exists between dust and synchrotron, being Galactic components, so that the hypothesis of statistical independence that the ICA algorithm requires to work is not properly satisfied.

Another aspect to note is that the precision of the reconstruction of CMB and radio sources is high, despite of their markedly different spatial statistics: Regarding this aspect, it is useful to test the goodness of the reconstruction of the radio sources signal by considering their number counts, represented as follows. Both in the input and output maps, we individuate maximum and minimum,  $s_{max}, s_{min}$ . Then we consider a fractional flux running from 0 to 1 defined as

$$\Delta s = \frac{s - s_{min}}{s_{max} - s_{min}}, \quad (33)$$

because this enables us to compare input map and reconstructed one directly. This has been done in figure 7, dashed and solid lines for input and output respectively: we plot the cumulative number of pixels exceeding a given value of  $\Delta s$ . The algorithm correctly recovers essentially all sources for  $\Delta s \geq 2 \times 10^{-2}$ , corresponding to a signal of about  $50\mu K$ ; this antenna temperature can be expressed as a flux  $I$  by using the usual formula  $I = (2k_B T / \lambda^2) \Delta \Omega$ , where  $T$  is the antenna temperature,  $k_B$  the Boltzmann constant,  $\lambda$  the wavelength and  $\Delta \Omega$  the solid angle covered by the source at the present resolution, that is  $3.5' \times 3.5' \simeq 10^{-6}$  sterad.: the result is about 15 mJy. Below this threshold, reconstructed counts are overestimated; this is probably due to the contamination from the other signals present in the input data. In any case, the flux limit for source detection is surprisingly low, substantially lower or at least comparable to that achieved with other methods which require stronger assumptions on the signals to recover (Cayón et al. 2000; Hobson et al. 1998); in fact, rms fluctuations from the CMB, that have to be considered as the main cause of noise for sources detection at these frequencies, are at the level  $\sigma_{CMB} \simeq 70\mu K$  at 100 GHz, that means that essentially all the sources have been recovered down to a flux limit corresponding to  $0.7\sigma_{CMB}$ . This high efficiency in detecting point sources illustrates the ability of the method in taking the maximum advantage of the different frequency and spatial properties of the signals present in the simulated maps: CMB is a realization of a Gaussian process, while radio sources are similar to a shot noise obeying a Poisson statistics. On the other hand, we stress that our approach is

idealized in a number of aspects: no beam convolution has been taken into account, and the same frequency scaling has been assumed for all sources. Therefore more detailed investigation are needed to assess the realistic source detection limit.

Finally note that, for all the signals, the same quality of the separation occurs at each scale, as it is evident in the bottom left panels, (except for the largest scales in the radio sources, because their true power spectrum goes to zero at low  $\ell$ 's more rapidly than the reconstructed one). This is a very important issue if we want to use an algorithm like this at the best resolution of a given experiment.

## 5.2 Frequency scaling recovery

Another new possibility in this framework is the recovery of the frequency scalings. Since we have seen that the spatial signals have been recovered rather well, it is expected that something could be recovered also about the frequency scalings, from the matrix  $W$  at the end of the separation process. Indeed, recalling that we write our outputs as  $\mathbf{u} = W\mathbf{x}$ , where  $\mathbf{x} = A\mathbf{s}$ , we mentioned that in the ideal case  $WA$  would assume a form of a diagonal matrix containing the constants  $d$  for all the signals, multiplied by a permutation matrix. It can be easily seen that if this is true by inverting the matrix  $W$  and performing the ratio, column by column, of each element with the one corresponding to the row at a given frequency, the frequency scalings of all the components are obtained, independently of the constants with which the signals have been recovered. However, as we showed in Section III, if some signals are much smaller than others the above reasoning would be only approximately valid. Indeed this is precisely our case, in which we are able to recover the frequency scaling of the strongest signals, CMB and radio sources, while the others are lost.

In Table 2 we compare these numbers with the theoretical ones computed from the true matrix  $A$  in table 1: we take the inverse of our final matrix  $W$  and we display each column divided by its element at the 100 GHz corresponding row. As it is evident, column 3 and 2 can be unambiguously identified as the frequency scalings of black body (CMB) and radio sources respectively, and with percent precision, while the other two columns do not resemble neither synchrotron nor dust.

We conclude here that our algorithm was successful in separating the signals we posed as inputs. The novelty that we think very interesting is the ICA approach implemented as a neural network: it allowed to gain the solutions without any assumption on the input components, and also to recover partially the frequency scalings; these are two extremely encouraging and new features of this approach.

## 6 CONCLUDING REMARKS AND FUTURE DEVELOPMENTS

Almost any observation in astrophysics results in a superposition of different emissions along the line of sight, from several physical processes that may be known with a certain approximation, or completely unknown. The only general thing that could be said in such a condition is that we can identify classes of components clearly uncorrelated one each

other, since ultimately their radiation is emitted at different places and times along our past light cone. Also, each component of the emitted radiation is scientifically interesting in almost all the cases.

It would be nice to have an algorithm able to exploit the independence of the signals composing the astrophysical sky maps at different frequencies and to recover each single component, with no hypothesis on the signals themselves except that each component is given by a product of a spatial pattern times a frequency function, even unknown. In this work we propose what we think is a good candidate to make this job, by introducing the ICA algorithm. The new feature of this approach is basically the capability of the algorithm to *learn*, following suitable criteria, how to recover the independent components that compose the input maps. The price of such a lack of *a priori* information is that each signal can be recovered multiplied by an unknown constant produced during the learning process itself. However this is not a substantial limitation, since a lot of physics is encoded in the spatial patterns of the signals, and ultimately the right normalization of each separated component can be obtained by matching with other independent observations.

Indeed, we demonstrate here that such framework works for astrophysical sky maps that are characterized, for our particular problem, by enhanced amplitude difference between components as well as markedly different spectral behaviors.

We develop a neural network suitable to implement the Independent Component Analysis (ICA) algorithm, and we apply it to simulated  $15^\circ \times 15^\circ$  portions of sky at 30,44,70,100 GHz, corresponding to the frequency channels of the future PLANCK Surveyor Low Frequency Instrument (LFI); the PLANCK mission, to be performed in a few years, is designed to definitively establish the properties of the anisotropies in the Cosmic Microwave Background (CMB) on the whole sky. This first application is interesting because at the LFI frequencies the sky contains dominant and small contributions, respectively from CMB and extragalactic radio sources and from Galactic contaminations due to thermal emission from 20 Kelvin dust and electromagnetic scattering between charged particles. This variety of signals, characterized by markedly different angular patterns and frequency scalings, allows us to give a good example of the application of the ICA algorithm in astrophysics.

The algorithm is able to perform separation taking a time which is of the order of 1 minute for  $15^\circ \times 15^\circ$  sky patches with  $3.5' \times 3.5'$  pixels on a 300 MHz - UltraSparc machine.

We show very interesting and promising results. CMB is recovered with percent precision. The algorithm is remarkably efficient also in the detection of extragalactic radio sources: under the present hypotheses, and at the present resolution of about  $3.5' \times 3.5'$ , almost all the sources brighter than 15 mJy at 100 GHz are recovered; this value is roughly  $0.7\sigma_{CMB}$ , where  $\sigma_{CMB}$  is the rms level of CMB fluctuations. The subdominant signals, with amplitude one or two order of magnitudes lower depending on frequency, are recovered at the 10% precision. Reconstruction possesses equal quality on all the scales of the input maps, up to the pixel size.

In addition, we show that the final outputs of the ICA process could be also used to recover the frequency scalings of the signals. This is achieved essentially by making ratios

**Table 2.** Output signals frequency scalings.

frequency channel (GHz)	column 1 synchrotron	column 2 radio sources	column 3 CMB	column 4 dust
100	1.00	1.00	1.00	1.00
70	1.36	1.95	1.14	.934
44	1.72	4.70	1.23	1.93
30	-12.0	9.70	1.26	3.77

between the column elements of the inverse of the ICA estimated matrix connecting input data to outputs. We show that for the dominant components again they are recovered at the percent precision, while for the subdominant ones this information is almost lost due to the worse quality of the reconstruction.

All this seems to be suitable of a wide use in astrophysics, essentially because in almost any experiment the observed sky patch contains a superposition of independent signals from different astrophysical processes, each one characterized by its own spatial pattern and frequency scaling.

Of course, much work has to be done to better explore our approach. First of all, it has to be tested for more realistic experiments, where the data are corrupted by noise and convolved with the instrumental beam shapes. We plan to do this first in the context of the PLANCK satellite experiment. In this precise case, the components we treated here are not the only that will appear in the observed data. Other foregrounds will contaminate the pure CMB signal, like *free-free* Galactic emission, far infrared extragalactic sources and source clustering, as well as interaction of the CMB itself with galaxy clusters. However, the nine frequency channels of the PLANCK satellite are potentially able to treat all these contributions. A problem that will have to be faced in the context of a realistic simulation is that the assumption that each astrophysical component can be modeled as a product of a map times a frequency scaling is not completely satisfied. Examples of this features are galactic dust, which temperature varies across the sky roughly from 18 to 25 Kelvin; also, the signal from extragalactic sources does not satisfy this hypothesis, since each one is expected to follow its own spectrum that may differ between different populations. Moreover, it has to be taken into account that the Galactic diffuse components are not completely statistically independent and this can reduce the efficiency of any separation algorithm making use of this hypothesis.

On the other hand, many improvements can still be introduced in this separation procedure. In the learning stage, the ICA algorithm makes use of non-linear functions that, case by case, are chosen to minimize the mutual information between the outputs; also in this case, a further improvement could be obtained by specializing the ICA inner non-linearities to treat our astrophysical task.

Another aspect to explore is how to improve the results by implementing the prior knowledge that we could have for some of the signals to recover. Indeed, although the main advantage of this neural network approach is the “blindness” of separation, at least for the PLANCK mission we should have several informations, both for spatial statistics and frequency scalings, that should be taken into account. This aspect regards both the extraction of the known components

from the data, as well as the denoising and deconvolution processes.

The study of all these aspects is in progress, and each one deserves a great work. However, it seems to us that our results show clearly the great potentiality of the implementation of the neural networks and Independent Component Analysis in astrophysics.

We warmly thank Luigi Danese for original suggestions.

We thank Krzysztof M. Górska and all the people who collaborated to build the HEALPix pixelization scheme extensively used in this work.

## REFERENCES

Amari S. & Chichocki A., 1998, Proc. IEEE 86 2026  
 Bell A.J. & Sejnowski T.J., 1995, Neural Computation 7 1129  
 Bennet, C. et al., 1996, Amer. Astro. Soc. Meet., 88.05  
 Bouchet F.R., Prunet S., Sethi S.K., 1998, astro-ph/9809353, MNRAS in press; Tegmark M., Efstathiou G., 1996, MNRAS 281, 1297  
 Cayón, L., Sanz, J.L., Barreiro, R.B., Martínez-González, E., Vielva, P., Toffolatti, L., Silk, J., Diego, J.M. & Argüeso, F., 2000, astro-ph/9912471, MNRAS, in press  
 Donoho, D.L. & Johnstone, I. M., 1995, Journal of the American Statistical Association, 90, 1200.  
 Fixsen, D.J., Cheng, E.S., Gales, J.M., Mather, J.C., Shafer, R.A., Wright, E.L., 1996, ApJ, 473, 576  
 Górska M., Wandelt B.D., Hansen F.K., Hivon E. & Banday A.J., 1999, astro-ph/9905275; see the HEALPix web page at <http://www.tac.dk:80/~healpix/>  
 Haslam C.G.T. et al., 1982, A& AS 47, 1  
 Hobson M.P., Barreiro R.B., Toffolatti L., Lasenby A.N., Sanz J.L., Jones A.W. & Bouchet F.R., 1999, astro/9810241, MNRAS 306, 232  
 Hobson M.P., Jones A.W., Lasenby A.N. & Bouchet F.R., 1998, astro-ph/9806387 MNRAS in press  
 Jawerth, B. & Sweldens, W., 1994, SIAM review, 36 (3), 377  
 Lemarié, P.G. & Meyer, Y., 1986, Rev. Mat. Ib., 2, 1  
 Mallat, S.G., 1989, IEEE Trans. Pat. Anal. & Mach. Int., 11, 674  
 Mandolesi, N. et al., 1998, PLANCK Low Frequency Instrument, A Proposal Submitted to the ESA for the FIRST/PLANCK Programme  
 Mather, J.C., Fixsen, D.J., Shafer, R.A., Mosier, C., Wilkinson, D.T., 1999, ApJ, 512, 511  
 Ogden, R.T., 1997, “Essential Wavelets for Statistical Applications and Data Analysis”, Birkhauser Boston  
 Puget, J. L. et al., 1998, High Frequency Instrument for the PLANCK Mission, A Proposal Submitted to the ESA for the FIRST/PLANCK Programme  
 Sanz, J.L., Argüeso, F., Cayón, L., Martínez-González, E., Barreiro, R.B. & Toffolatti, L., 1999, MNRAS, 309, 672  
 Sanz, J.L., Barreiro, R.B., Cayón, L., Martínez-González, E., Ruiz, G.A., Díaz, F.J., Argüeso, F., Silk, J. & Toffolatti, L., 1999, A&A, 140, 99

Schlegel D.J., Finkbeiner D.P. & Davies M., 1998, ApJ 500, 525  
 Seljak U., Zaldarriaga M., 1996, ApJ 469, 437  
 Skilling J., 1989, in Skilling J., ed., *Maximum Entropy and Bayesian Methods*. Kluwer, Dordrecht, p. 53; Skilling J., 1988, in G. J. Erickson ,C.R. Smith eds ., *Maximum Entropy and Bayesian Methods in Science and Engineering*. Kluwer, Dordrecht, v.1, p. 173; see also Gull S.F., *Bayesian Inductive Inference and Maximum Entropy Method*, on the same text, p. 53.  
 Smoot G.F. et al., 1992, ApJL L1  
 Tegmark M., de Oliveira-Costa A., 1998, astro-ph/9802123, ApJ 500 L83  
 Tegmark M., Eisenstein D.J., Hu W., & De Oliveira-Costa A., 1999, astro-ph/9905257, ApJ in press 1999  
 Tenorio, L., Jaffe, A.H., Hanany, S. & Lineweaver, C.H., 1999, astro-ph/9903206, MNRAS, submitted  
 Toffolatti L., Argüeso F., De Zotti G., Mazzei P., Franceschini A., Danese L., Burigana C., 1998, MNRAS, 297, 117  
 Turner M.S., Tyson J.A., 1999, astro-ph/9901113, Rev.Mod.Phys. 71 S145  
 Yang H.H. & Amari S., 1997, Neural Computation 9 1457

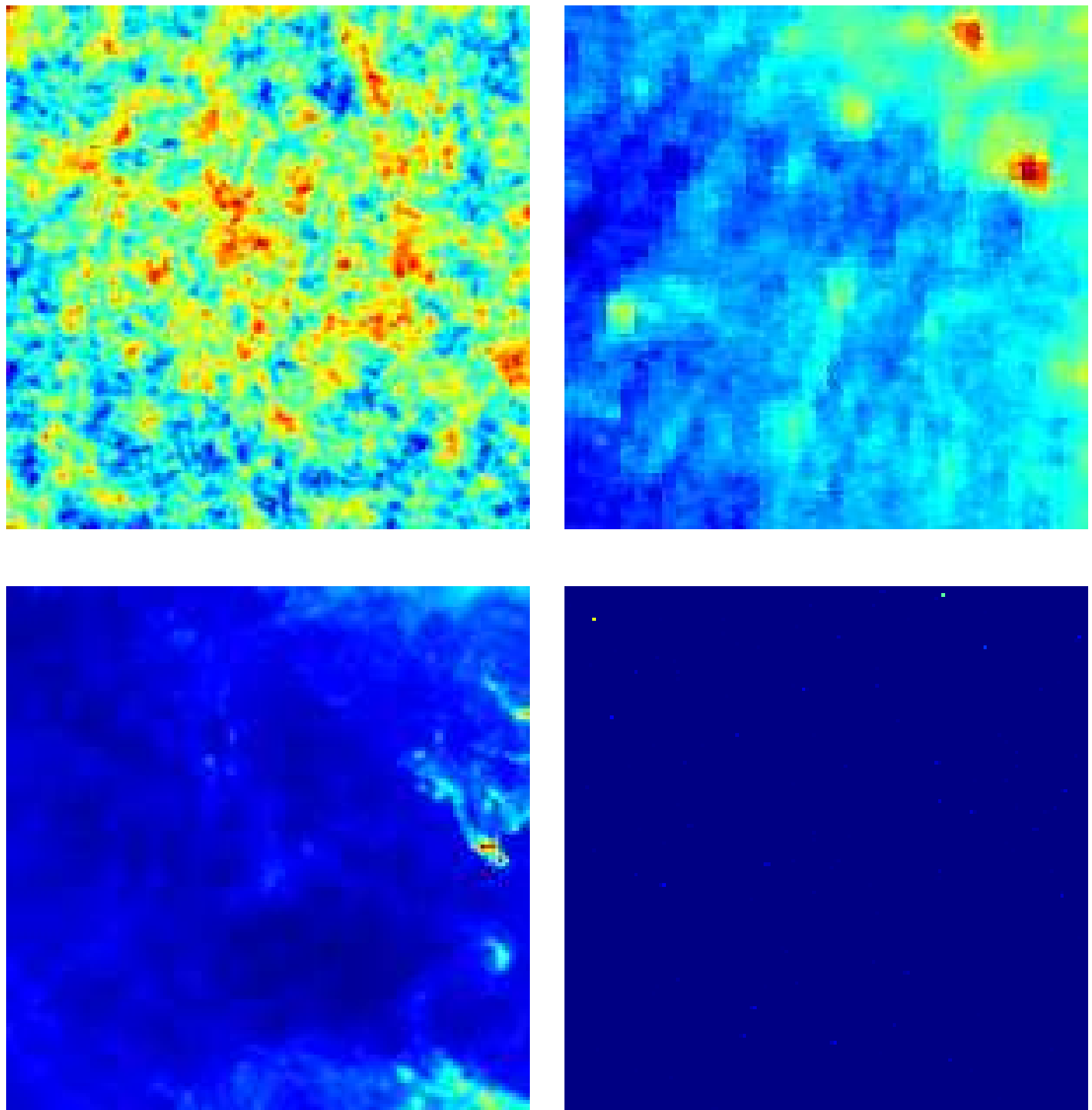


**Figure 1.** This figure shows the inputs used in the ICA separation algorithm: from top left, in a clockwise sense, the maps represent simulation of CMB, synchrotron, radio sources and dust emission.

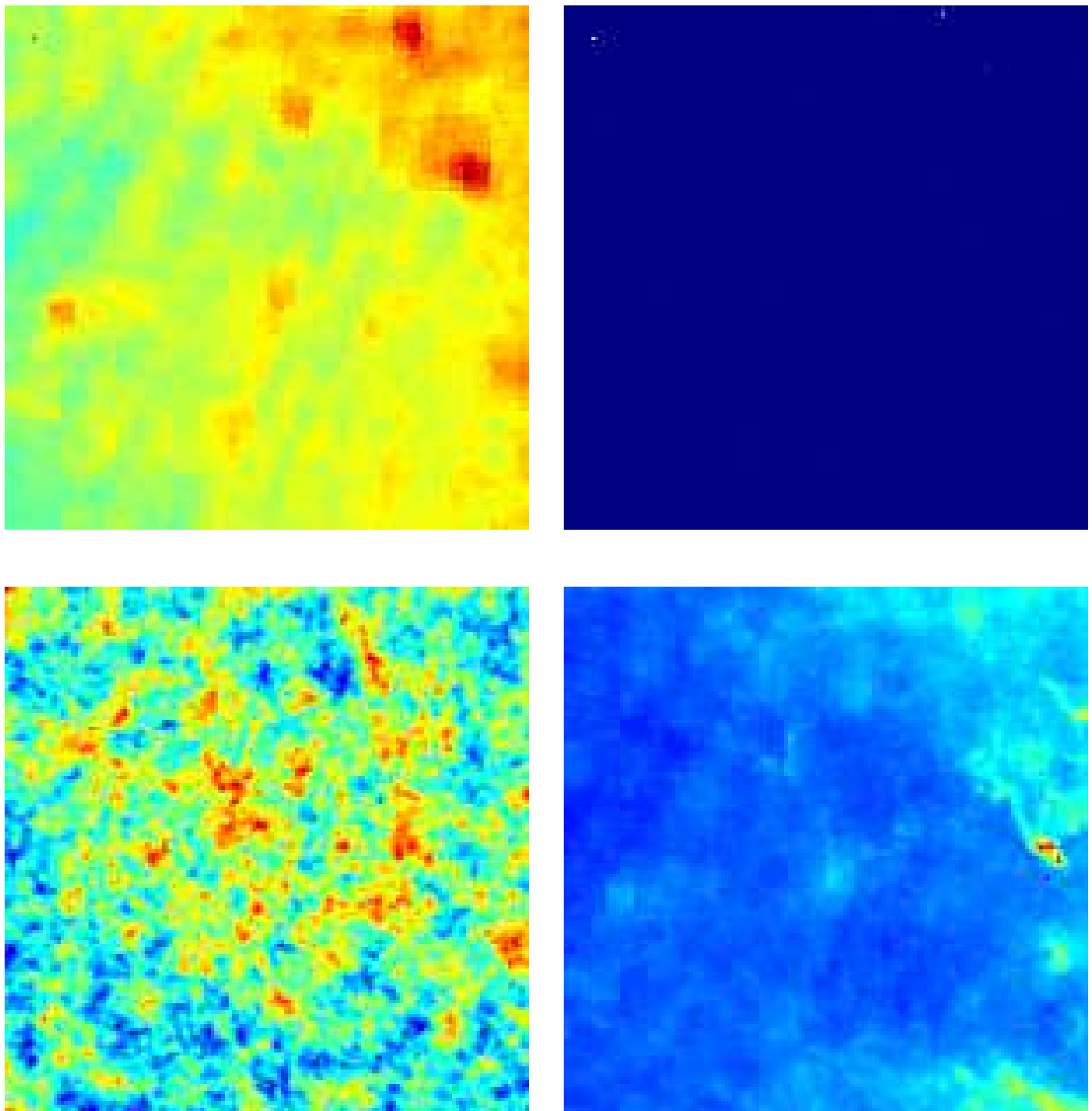


**Figure 2.** Output signals: these are the reconstructed maps produced by the ICA method; the initial ordering has not been conserved in the outputs. From top left, in a clockwise sense, we can recognize synchrotron, radio sources, dust and CMB.

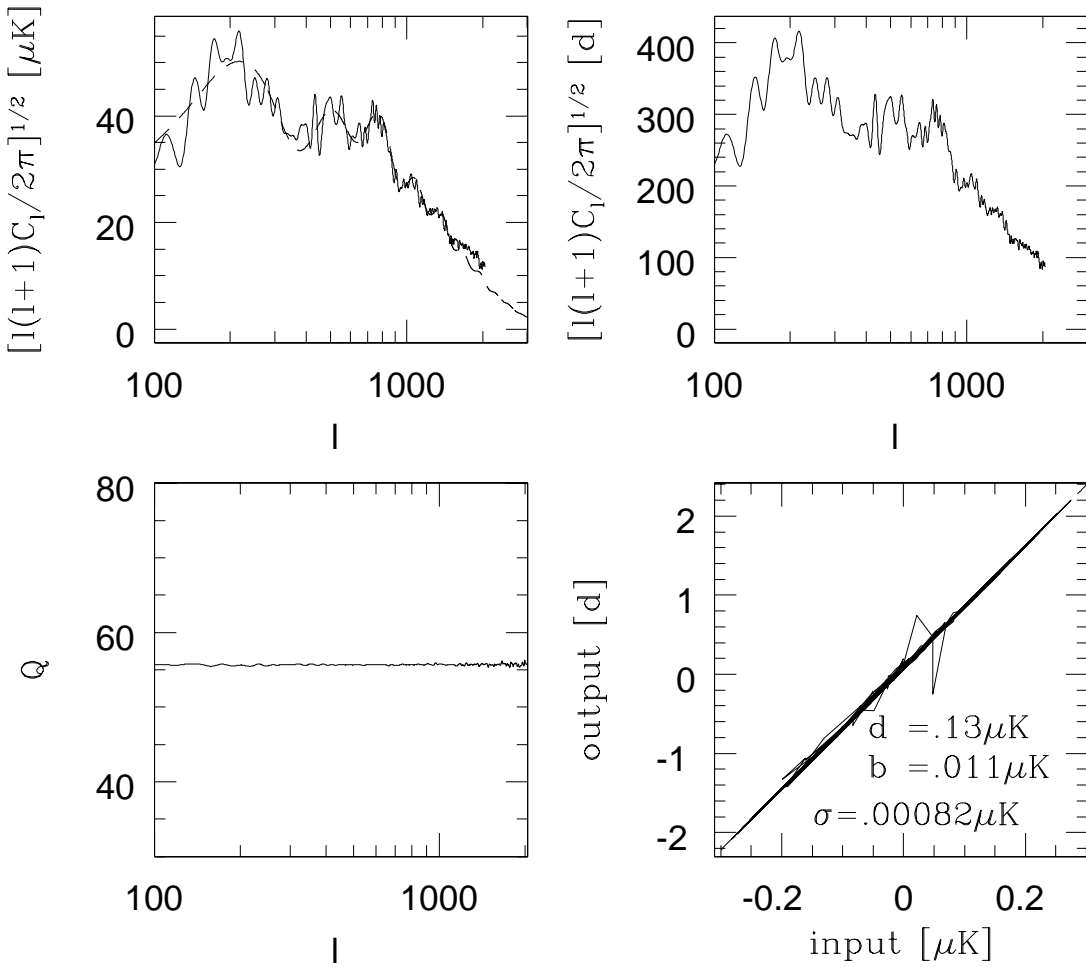


**Figure 3.** CMB analysis. Top left: input angular power spectra, simulated (solid line) and theoretical (dashed line, see text). Top right: the angular power spectrum of the reconstructed CMB patch. Bottom left: quality factor relative to the input/output angular spectra. Bottom right: scatter plot and linear fit (dashed line) for the CMB input/output maps.

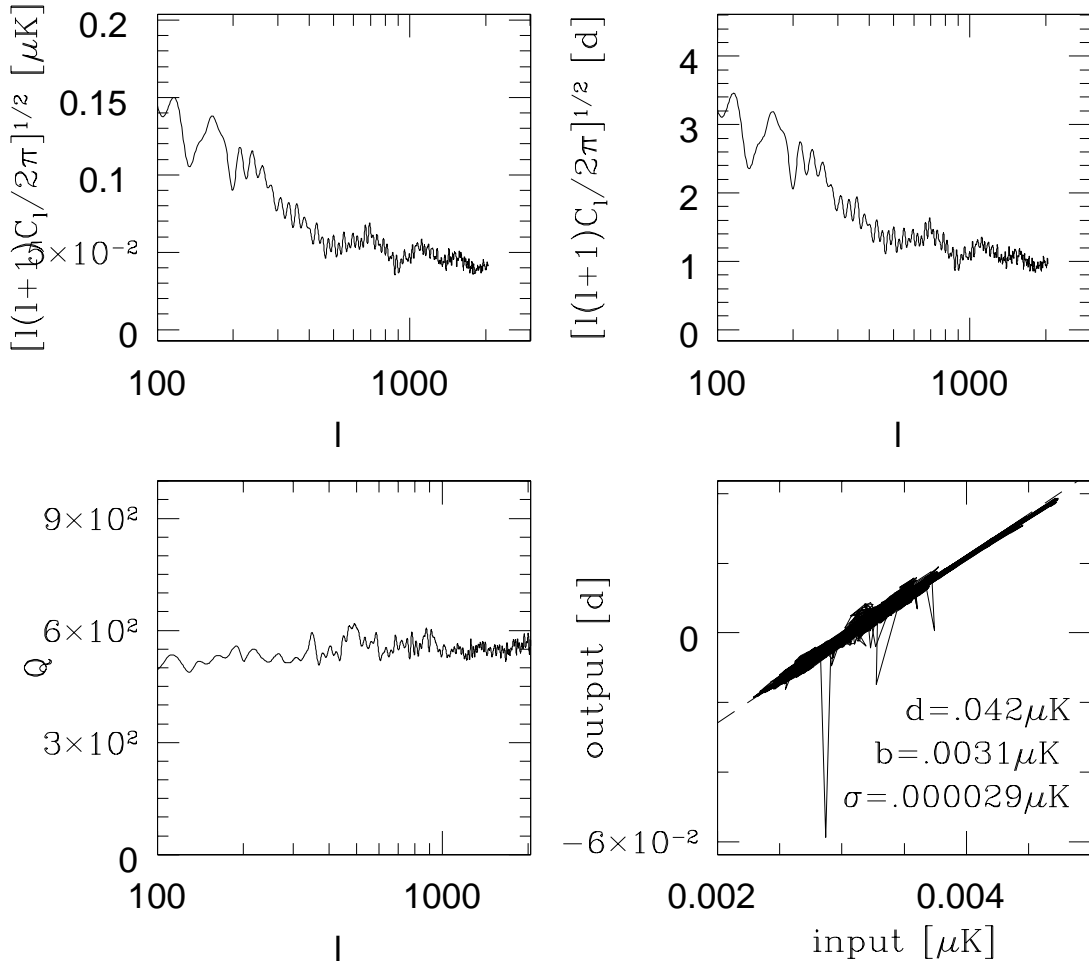


**Figure 4.** Synchrotron analysis. Top left: angular power spectra for the simulated input synchrotron map; top right: angular power spectrum of the reconstructed synchrotron patch. Bottom left: quality factor relative to the input/output angular spectra. Bottom right: scatter plot and linear fit (dashed line) for the synchrotron input/output maps.

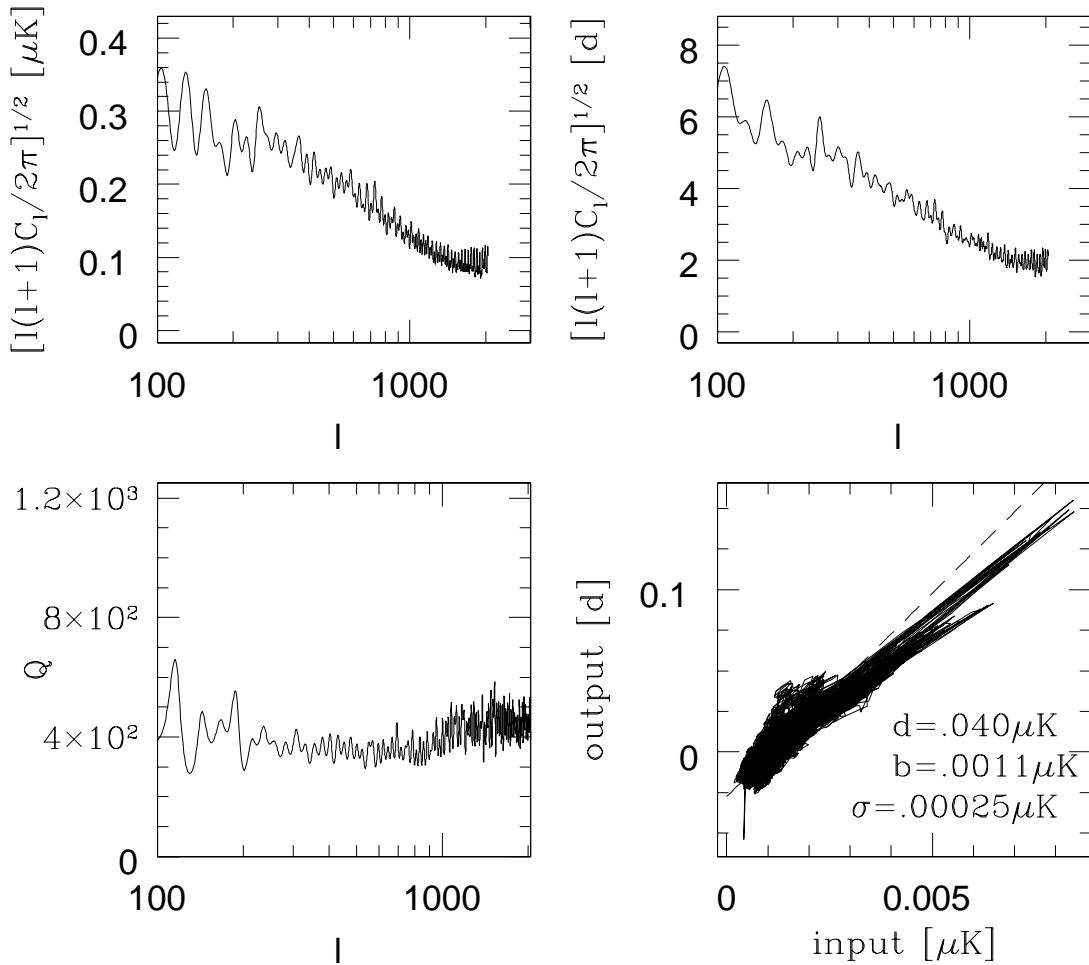


**Figure 5.** Dust analysis. Top left: angular power spectra for the simulated input dust emission map; top right: angular power spectrum of the reconstructed dust emission patch. Bottom left: quality factor relative to the input/output angular spectra. Bottom right: scatter plot and linear fit (dashed line) for the dust input/output maps.

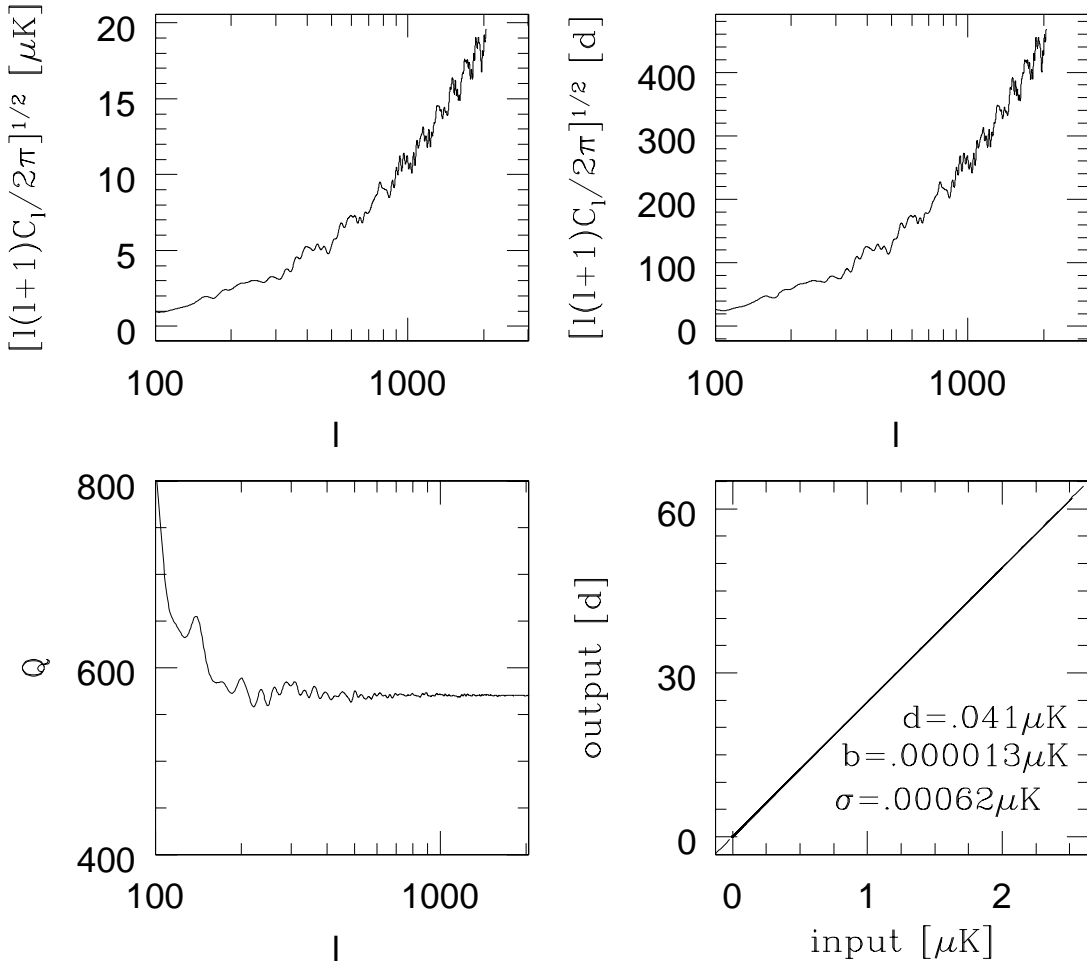


**Figure 6.** Radio sources analysis. Top left: angular power spectra for the simulated emission of radio sources map; top right: angular power spectrum of the reconstructed radio sources emission map. Bottom left: quality factor relative to the input/output angular spectra. Bottom right: scatter plot and linear fit (dashed line) for the radio source emission input/output maps.

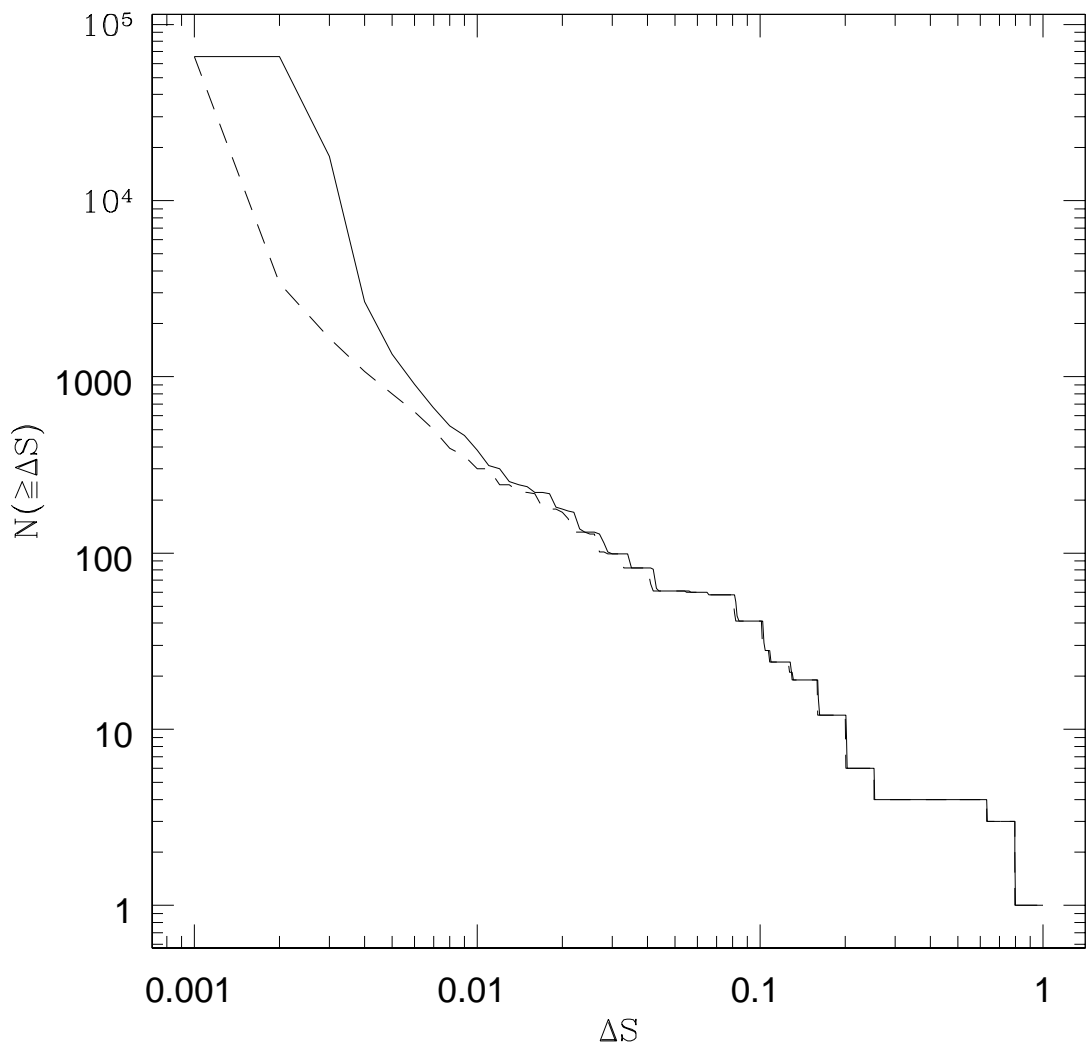


**Figure 7.** Cumulative number of pixels as a function of the threshold  $\Delta s$  (see text for more details): input (dashed line) versus output (solid line).